Available online at www.sciencedirect.com
SCIENCE DIRECT®
Carbon 42 (2004) 2057–2066
CARBON
www.elsevier.com/locate/carbon

Band structure and transport properties of carbon nanotubes using a local pseudopotential and a transfer-matrix technique

A. Mayer *

Laboratoire de Physique du Solide, Facultés Universitaires Notre-Dame de la Paix, Rue de Bruxelles 61, B-5000 Namur, Belgium

Received 28 October 2003; accepted 9 April 2004
Available online 18 May 2004

Abstract

In order to address the band-structure and transport properties of carbon nanotubes, we build a local pseudopotential from the requirement that results relevant to the π-bands of simple hexagonal graphite and isolated graphene sheets are reproduced. We then apply a transfer-matrix technique to compute the band structure and conductance of the (10,0), (5,5), (10,10), (15,15) and (10,10)@(15,15) carbon nanotubes. We also investigate how the conductance of a broken (10,10) nanotube is affected by a (15,15) tube placed around the gap. Our results show how fast band-structure and stationary-wave effects appear in finite-size nanotubes. They provide a complementary insight on the effects of the tubes' curvature and the transferability of parameters from graphite to carbon nanotubes.

Keywords: A. Carbon nanotubes; B. Theory; D. Transport properties

1. Introduction

The transfer-matrix methodology is one of the techniques used to derive scattering solutions in situations where the relevant propagation equations are linear. The physical systems to which it applies are those located between two separate boundaries, standing for the regions of incidence and transmission. Given a set of boundary states used for the expansion of the wave function in these two regions, the transfer matrices provide for each incident state the coefficients of the corresponding transmitted and reflected states.

The technique has been developed by many authors, including Bayman [1], Tamura [2], Pendry [3–7], Palacios [8], Wu [9], Sheng [10,11], Price [12], Kostyrko [13], Andriotis [14], Choi [15] and ourself [16–18]. Its computation time grows as the cube of the number of basis states used for the expansion of the wave function (because of the matrix multiplications). This number depends on the lateral size of the system and the cut-off energy. The number of states one has to consider simultaneously can however be reduced significantly if symmetries are present [18]. The computational effort required to propagate these states through the system is simply proportional to its length, which constitutes the main advantage of the technique. In situations where the system is periodic, the procedure is still more efficient as one can use repeatedly the transfer matrices associated with a single cell. If N is the number of basic cells one wants to consider and if an algorithm based on the binary decomposition of N is used, the computational time turns out to depend on $\log N$.

Using the layer-addition algorithm [2–4] enables one to control the stability of the procedure [16] and address periodic repetitions of a given cell. The "closed" or "quasi-bound" states, which only exist in the intermediate region, influence the transmission of the "open" scattering states and must be considered. That issue was discussed by others [1,9–12] and several solutions were proposed to remove them from the final expressions, where only propagating states subsist. Our specific approach regarding that point is to use non-square transfer matrices at the boundaries [17], thus imposing a physical reflection to those closed states and preventing numerical instabilities.

* Tel.: +32-817-247-20; fax: +32-817-24-707.
E-mail address: alexandre.mayer@fundp.ac.be (A. Mayer).
URL: http://www.fundp.ac.be/simamayer.

0008-6223/$ - see front matter © 2004 Elsevier Ltd. All rights reserved.
doi:10.1016/j.carbon.2004.04.017

Transfer matrices are generally applied in electromagnetism or in the study of electronic wave guides having defects or being subject to magnetic fields. For a few years they are also applied to carbon nanotubes [7,13–15]. In situations where the wave function must be determined not only inside but also outside the nanotube, a real-space formulation of the technique is appropriate. Pseudopotentials are then used for the representation of each atom [15]. In this paper, we build a pseudopotential that is local and suited to a one-electron approach, and address the transport properties of carbon nanotubes. After a presentation of key aspects of the transfer-matrix methodology in Section 2, we construct in the following section the pseudopotential from the requirement that it reproduces the π-bands of simple hexagonal graphite and isolated graphene sheets. We then apply in Section 4 these techniques to the computation of the band structure and conductance of the (10,0), (5,5), (10,10), (15,15) and (10,10)@(15,15) nanotubes. We also investigate how the conductance of a broken (10,10) nanotube is affected by a (15,15) tube placed around the gap. Our results turn out to be in excellent agreement with those obtained using other techniques and show how fast band-structure and stationary-wave effects appear in finite-size nanotubes. They provide a complementary insight on the effects of the tubes' curvature and the transferability of parameters from graphite to carbon nanotubes.

2. Theory

We present here the main lines of the technique used to derive the scattering solutions and band structures presented here-after. Let us consider the system depicted in Fig. 1. It consists of three parts: Region I ($z \leqslant 0$), Region II ($0 \leqslant z \leqslant D$) that contains the scattering strengths, and Region III ($z \geqslant D$). We refer by $\{\Psi_j^{\mathrm{I/III},\pm}\}$ to the basis states used to expand the wave function in Regions I and III, for a given value of the energy E. The ± sign refers to the propagation direction relative to the z axis and the subscript j enumerates the parameters $\{k_\rho, m\}$ that characterize each basis state in cylindrical coordinates. Our objective is to determine how states incident on one side of Region II are scattered towards the other.

2.1. Derivation of scattering solutions

In order to reach that objective, we start by establishing solutions associated with single outgoing $\Psi_j^{\mathrm{III},+}$ or incoming $\Psi_j^{\mathrm{III},-}$ states in Region III. Since the wave function and its derivatives are entirely defined in Region III, one can propagate these states numerically [19–22] from $z = D$ to $z = 0$, where the solutions are expanded in terms of incident $\Psi_j^{\mathrm{I},+}$ and reflected $\Psi_j^{\mathrm{I},-}$

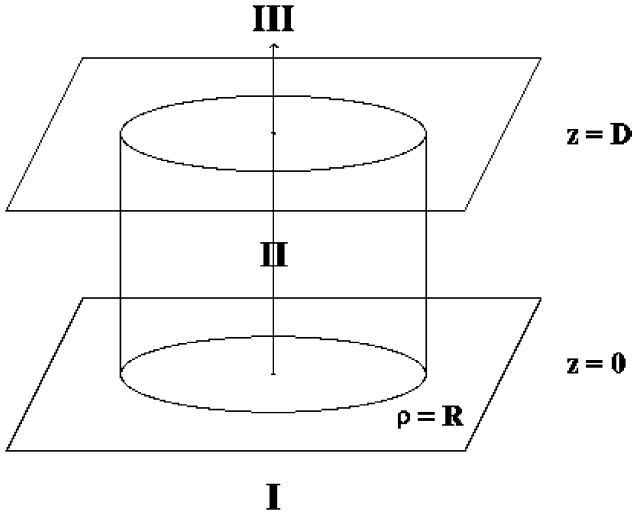

Fig. 1. Schematic representation of the situation considered. Regions I and III are the regions of incidence and transmission. The intermediate Region II contains the basic cell of the nanotubes.

states. The coefficients of these expansions are stored in $\mathbf{T}^{\pm,\pm}$ matrices and we thus establish the following set of solutions:

$$\overline{\Psi}_j^{+z\leqq 0} \sum_i T_{i,j}^{++} \Psi_i^{\mathrm{I},+} + \sum_i T_{i,j}^{-+} \Psi_i^{\mathrm{I},-z\geqq D} \Psi_j^{\mathrm{III},+}, \tag{1}$$

$$\overline{\Psi}_j^{-z\leqq 0} \sum_i T_{i,j}^{+-} \Psi_i^{\mathrm{I},+} + \sum_i T_{i,j}^{--} \Psi_i^{\mathrm{I},-z\geqq D} \Psi_j^{\mathrm{III},-}. \tag{2}$$

Due to the linearity of the propagation equations, one can consider combinations of those expressions and establish scattering solutions associated with either a single incident state $\Psi_j^{\mathrm{I},+}$ in Region I or a single incident state $\Psi_j^{\mathrm{III},-}$ in Region III. Formally these new solutions are expressed in terms of $\mathbf{S}^{\pm,\pm}$ matrices in the following way:

$$\Psi_j^{+z\leqq 0} \Psi_j^{\mathrm{I},+} + \sum_i S_{i,j}^{-+} \Psi_i^{\mathrm{I},-z\geqq D} \sum_i S_{i,j}^{++} \Psi_i^{\mathrm{III},+}, \tag{3}$$

$$\Psi_j^{-z\leqq 0} \sum_i S_{i,j}^{--} \Psi_i^{\mathrm{I},-z\geqq D} \Psi_j^{\mathrm{III},-} + \sum_i S_{i,j}^{+-} \Psi_i^{\mathrm{III},+}. \tag{4}$$

The $\mathbf{S}^{\pm,\pm}$ matrices, which contain the coefficients of the transmitted and reflected states, are obtained directly from the $\mathbf{T}^{\pm,\pm}$ matrices established previously using [4] $\mathbf{S}^{++} = \mathbf{T}^{++^{-1}}$, $\mathbf{S}^{-+} = \mathbf{T}^{-+}\mathbf{T}^{++^{-1}}$, $\mathbf{S}^{--} = \mathbf{T}^{--} - \mathbf{T}^{-+}\mathbf{T}^{++^{-1}}$ $\mathbf{T}^{+-}$ and $\mathbf{S}^{+-} = -\mathbf{T}^{++^{-1}}\mathbf{T}^{+-}$.

The numerical instabilities that appear when D is too large (because of the inversion of $\mathbf{T}^{++}$) are controlled by splitting Region II into smaller segments and treating them separately. The $\mathbf{S}^{\pm\pm}$ matrices associated with the complete system are obtained using the combination rules given in Refs. [2–4,16]. In order to deal with another source of instabilities, the $\mathbf{T}^{\pm\pm}$ and $\mathbf{S}^{\pm\pm}$ matrices of Eqs. (1)–(4) should only connect propagating states in

Regions I and III. As additional states are however required to represent accurately the wave function in the intermediate Region II, specific techniques are required to match the solutions at $z = 0$ and $z = D$. We deal with that point by considering a reference potential sufficiently low to have only propagative boundary states at the limits of each segment in Region II. The connection with the "external states" at $z = 0$ and $z = D$ is then achieved using non-square transfer matrices [17], thus imposing a physical reflection to the "internal states".

2.2. Derivation of the band structure of periodic materials

Let us now consider the basic cell of a periodic material. For each value of the energy E, one can compute the transfer matrices that describe its scattering solutions. The Bloch states that define the band structure of the material are those that keep unchanged after propagation through one period a of the material, except for the phase factor $e^{ik_z a}$. If we assume that the basis states $\Psi_j^{\mathrm{I},\pm}$ and $\Psi_j^{\mathrm{III},\pm}$ have the form $\psi_j(\rho,\phi)\exp(\pm ik_{z,j}z)$, the Bloch states are actually found by solving the following generalized eigenvalue problem [4]:

$$\begin{pmatrix} \mathbf{S}^{++} & 0 \\ -\mathbf{S}^{-+} & \mathbf{I} \end{pmatrix}\mathbf{X} = \lambda \begin{pmatrix} \mathbf{I} & -\mathbf{S}^{+-} \\ 0 & \mathbf{S}^{--} \end{pmatrix} \times \mathbf{diag}[e^{-ik_{z,j}a},\ldots,e^{ik_{z,j}a}]\mathbf{X}, \quad (5)$$

where $\mathbf{I}$ is the identity matrix and $\mathbf{diag}[]$ stands for a diagonal matrix containing the elements in brackets. The eigenvalues λ that are relevant to the band structure are those that satisfy $|\lambda| = 1$ (considering the limited accuracy of the computation). Each eigenvalue then defines one point (k_z, E) of the band structure (through $\lambda = e^{ik_z a}$), while the corresponding eigenvector $\mathbf{X}$ contains the coefficients of the Bloch states at $z = 0$. The k_z values found using that procedure are automatically restricted to the first Brillouin zone $[-\pi/a, \pi/a]$ of the material.

3. Construction of a local pseudopotential for reproducing the π-bands of simple hexagonal graphite and isolated graphene sheets

In order to apply this transfer-matrix technique to carbon nanotubes, one needs a pseudopotential for the representation of the carbon atoms. In order to meet the specificities of our formalism, the pseudopotential has to be local and suited to a one-electron approach (the pseudopotentials developed for the density functional theory are non-local and meant to be used by many-electrons techniques). Since we are interested by the conduction properties of carbon nanotubes, we require more specifically the pseudopotential to be representative of the π-electrons.

Following the standard approach, we build the pseudopotential so that it reproduces results obtained with graphite (with geometric parameters taken from Ref. [23]). Keeping in mind that it will be applied hereafter to nanotubes, we will focus essentially on the Γ, K and M points of the first Brillouin zone. As explained in the paper by Charlier et al. [24], there are non-negligible interactions between the layers of graphite, which are responsible for the energies of these three points to be raised by 0.75 eV compared to the Fermi level. To account for these interactions, we impose the pseudopotential to reproduce results obtained for both graphite and isolated graphene sheets. These additional constrains actually fix the width of the pseudopotential and improve the reliability of the technique when applied to single-wall and multi-wall nanotubes.

The results we seek to reproduce are those given by the tight-binding model of Charlier et al. [24], whose parameters are determined from the DFT calculations of Ref. [23]. This model indeed provides an analytical expression for the π-bands of simple hexagonal graphite (AAA stacking), which accounts for inter-layer interactions. As these interactions are clearly manifested along the edge KH of the first Brillouin zone, we will include it in our representations. Finally following experimental data [25,26], we fix the position of the Fermi level of graphite by assuming a work function of 4.6 eV.

We assume that the pseudopotential associated with each atom has the form $V(r) = \sum_{i=1}^{3} A_i \exp(-a_i r^2)$, where r is the distance to the nucleus. Using a gaussian basis is convenient when computing the Fourier components of the potential energy and gives this latter a finite range (which is appropriate for neutral atoms). Other functions could complete this basis. For given values of the parameters A_i and a_i, we can apply standard plane-wave techniques [27] and compute the energies at the Γ, K, M and H points of the first Brillouin zone for both the simple hexagonal graphite and isolated graphene sheets (which are actually represented by simple hexagonal graphite with a double interlayer spacing). The construction procedure consists therefore in a Monte Carlo research of the parameters that provide the best agreement with the results of Charlier et al. [23,24]. The values we found for A_1, A_2 and A_3 are 10.607, 29.711 and −98.911 eV respectively, while the parameters a_1, a_2 and a_3 take the value of 0.12126, 1.9148 and 0.60078 r_{Bohr}^{-2} respectively.

The result of the fit is represented in Fig. 2, where the π-bands given by the tight-binding model of Charlier are compared with those obtained using the pseudopotential. There is a good agreement between the two models, except at high energies and along the edge KH in the first Brillouin zone of graphite where the energy should decrease because of interactions between neighboring layers [24]. This poor reproduction of the bands along

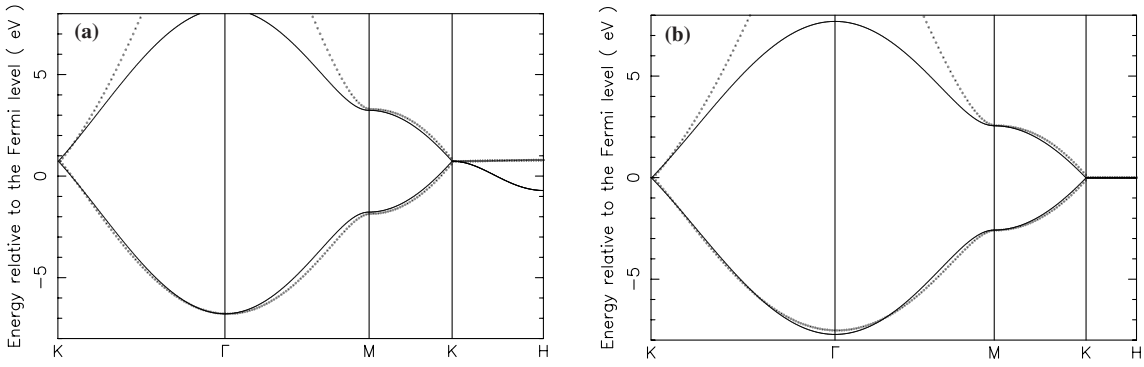

Fig. 2. Band structure of simple hexagonal graphite (left) and isolated graphene sheets (right), as calculated by a tight binding model (solid) and using a local pseudopotential (dots). The Fermi level is 4.6 eV below the vacuum level.

KH can be traced to the absence of non-local interactions in our model and explains why we did not consider other forms of graphite [28]. We however managed to raise satisfactorily the bands in the K–Γ–M plane of graphite, which is achieved by letting the pseudopotential be positive when r exceeds 0.12 nm. Considering that our main objective is to address conduction properties of carbon nanotubes, which are essentially determined by the π-bands of the K–Γ–M plane at energies close to the Fermi level, the fit is quite satisfactory. Indeed the mean error at the K, M and lower Γ points is 0.036 eV only. The pseudopotential should however not be used with systems whose configuration is not that of graphite (three neighboring carbons for each atom with a bonding length around 0.142 nm). For those systems, tight-binding Hamiltonians with intersystem hopping parameters [29–33] will provide better results. Indeed they can easily describe non-local interactions along the KH edge of graphite where our technique fails to be accurate and they have the advantage to include by construction the angular dependence of the π orbitals. The pseudopotential is however appropriate for the nanotubes considered hereafter, as demonstrated by the comparisons with the tight-binding formalism. It is also useful in situations where the wave function must be calculated in distant vacuum regions (as an expansion in terms of atomic orbitals is not pertinent in those regions).

4. Band-structure and transport properties of carbon nanotubes

Once the pseudopotential has been constructed, one can compute band-structure and transport properties of carbon nanotubes. Following previous publications [19–22], we adopt cylindrical coordinates and assume that the electrons involved by scattering are confined in a cylinder with radius R, which encloses the nanotube. The boundary states of Section 2 take therefore the form

$$\Psi_{m,j}^{\mathrm{I/III},\pm}(\rho,\phi,z) = \frac{J_m(k_{m,j}\rho)\exp(\mathrm{i}m\phi)}{R^{-1}\sqrt{2\int_0^R \mathrm{d}\rho\rho[J_m(k_{m,j}\rho)]^2}} \times \exp\left(\pm\mathrm{i}\sqrt{\frac{2m}{\hbar^2}E - k_{m,j}^2}z\right), \quad (6)$$

where J_m are Bessel functions, the radial wave vectors $k_{m,j}$ are solutions of $J'_m(k_{m,j}R) = 0$ and E is defined as the kinetic energy in Regions I and III (those two regions are described as perfect metals with a constant potential energy 25 eV lower than the vacuum level).

As the basis states are normalized so that the integration of $|\Psi_{m,j}^{\mathrm{I/III},\pm}|^2$ gives one electron per unit volume, the conductance [34] is computed using

$$G(E) = \frac{\mathrm{d}I}{\mathrm{d}V} = \frac{2e^2}{h}\sum_{(m',j'),(m,j)}\frac{v_{\mathrm{III},(m',j')}}{v_{\mathrm{I},(m,j)}}|S^{++}_{(m',j'),(m,j)}|^2, \quad (7)$$

where $v_{\mathrm{I/III},(m,j)} = \frac{\hbar}{m}\sqrt{\frac{2m}{\hbar^2}E - k_{m,j}^2}$ are the group velocities in Regions I and III and the summation only includes propagative states.

To obtain accurate results, the pseudopotentials have to be sampled with a resolution of 0.005 nm and it is sufficient to take R larger by 0.34 nm than the nanotube's radius. The number of wave vectors $k_{m,j}$ is determined by the condition $\hbar^2k_{m,j}^2/2m \leqslant E$ in Regions I and III and by $\hbar^2k_{m,j}^2/2m \leqslant E + \Delta E$ in the intermediate Region II where the nanotube is present. The parameter ΔE acts as a cut-off energy and determines the number of additional basis states that are required in Region II in order to reach a satisfactory representation of the wave function. We obtained stable results using $\Delta E = 200$ eV. Finally the results obtained using $J'_m(k_{m,j}R) = 0$ as boundary condition appeared identical with those obtained imposing $J_m(k_{m,j}R) = 0$, although convergence seems slightly faster using the first condition.

We will consider exclusively $(n,0)$ and (n,n) nanotubes, which are characterized by a central n-fold axis and reflection symmetries. As explained in Ref. [18], the n-fold symmetry enables one to separate the basis states into n independent groups (the potential coupling only states whose m values are separated by an integer multiple of n). Taking account of the reflection symmetries leads to further improvements, since the Fourier components of the potential and the corresponding coupling elements are pure real numbers instead of being complex. It turns out that the m values to consider in order to reach satisfactory results can be limited to those satisfying $|m| \leqslant 5 \cdot n$.

4.1. Band-structure and transport properties of the (10,0) nanotube

We start by considering the semiconducting (10,0) nanotube, whose configuration and band structure are represented in Figs. 3 and 4. The energy values are counted from the Fermi level, whose position is fixed by the middle of the gap. Compared to graphite, the Fermi level of the (10,0) nanotube turns out to be 0.25 eV higher (which means that its work function is 0.25 eV smaller). In the framework of our model, we explain this difference by the curvature of the nanotube and the long-range repulsive part of our pseudopotential (remember that its extension is sufficient to raise the electrons' energy by 0.75 eV at a distance of 0.335 nm). The tube's curvature is indeed responsible for the atoms being closer than in the flat planes of graphite, which makes them more feel the neighborhood's potential more strongly.

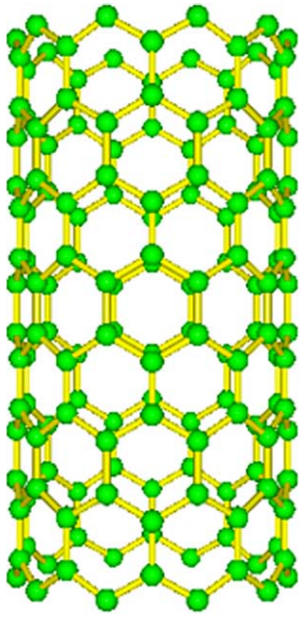

Fig. 3. Structure of the (10,0) nanotube. Only four basic units are represented.

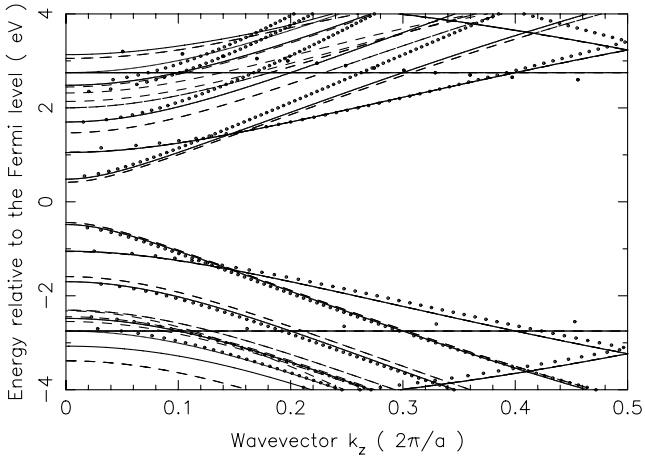

Fig. 4. Band structure of the (10,0) nanotube, as given by tight-binding models, using either the π-orbital approximation (solid) or a complete $sp_xp_yp_z$ basis (dashed), and as calculated using the pseudopotential (dots).

Fig. 4 reveals an excellent agreement between the results obtained using our local pseudopotential and those given by tight-binding models using either the π-orbital approximation [35] or a complete $sp_xp_yp_z$ basis [23]. The only significant discrepancies with the π-orbital model occur when the energy is higher than the Fermi level by at least 2 eV, as already observed with graphite. While the pseudopotential was build using the hopping parameter $\alpha_0 = 2.569$ eV in graphite [23], the best general agreement between our results and those provided by the two tight-binding models is achieved using as hopping parameter γ_0 ($V_{pp\pi}$) the experimental value of −2.75 eV. The gap-width found using our technique is 1.04 eV, which is very close to the value of 0.966 eV given by the π model and that of 1.015 eV provided by the model of Moussaddar et al. [36], where $\gamma_0 = -3.033$ eV and deformation potentials are taken into account.

Fig. 5 illustrates the conductance $G(E)$ of eight and 16 basic units of the (10,0) nanotube. Besides addressing finite-size effects, the result also accounts for reflections at the interface between the nanotube and the two metallic contacts. The figure shows that a nanotube consisting of eight units (i.e., twice the number represented in Fig. 2) already displays the essential conduction properties of infinite structures, which are essentially characterized by the band-gap and van Hove singularities [37]. For 16 units, these band-structure effects are perfectly defined. The figure also reveals other oscillations, whose number is proportional to the length of the tube and which come from stationary waves in the nanotube. Looking at the conductance at the Fermi level, one finds that it decreases exponentially with the length of the tube, each basic cell being responsible for a reduction by a factor of 1.93.

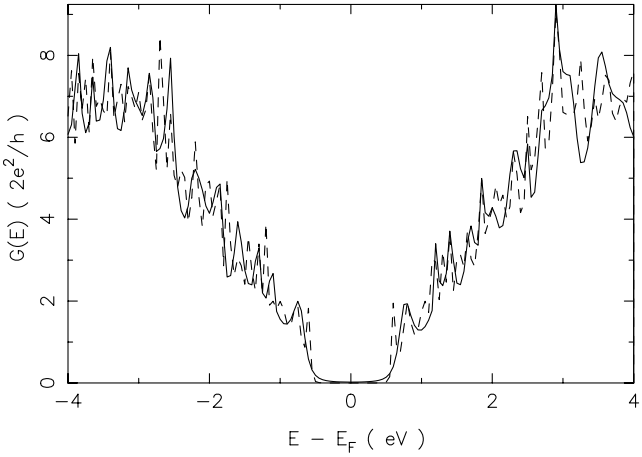

Fig. 5. Conductance of eight (solid) and 16 (dashed) basic units of the (10,0) nanotube. The results account for reflections at the metallic contacts that surround the tubes.

4.2. Band-structure and transport properties of the (5,5), (10,10) and (15,15) nanotube

Let us now consider the metallic (5,5), (10,10) and (15,15) nanotubes. We represented the configuration of the (5,5) in Fig. 6, and the band structure of the three nanotubes in Figs. 7–9. The energy values are counted from the Fermi level, whose position is fixed by the band crossing around $\frac{2}{3}\pi/a$. Compared to graphite, the Fermi level of the (5,5), (10,10) and (15,15) nanotubes turns out to be 0.34, 0.11 and 0.075 eV higher. These upwards displacements in the position of the Fermi level are again related to the extension of the pseudopotential

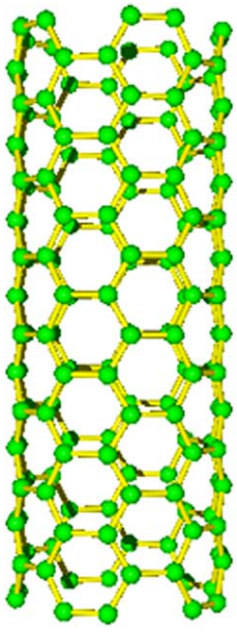

Fig. 6. Structure of the (5,5) nanotube. Only eight basic units are represented.

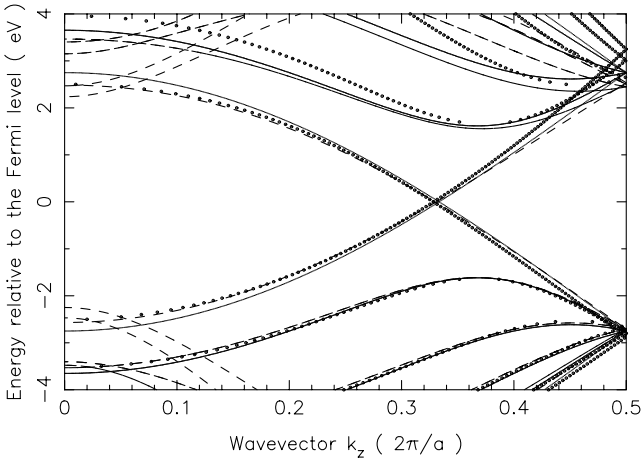

Fig. 7. Band structure of the (5,5) nanotube, as given by tight-binding models, using either the π-orbital approximation (solid) or a complete $sp_xp_yp_z$ basis (dashed), and as calculated using the pseudopotential (dots).

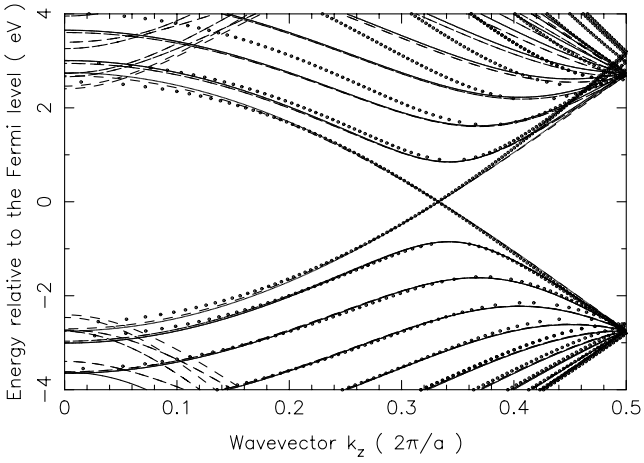

Fig. 8. Band structure of the (10,10) nanotube, as given by tight-binding models, using either the π-orbital approximation (solid) or a complete $sp_xp_yp_z$ basis (dashed), and as calculated using the pseudopotential (dots).

and the curvature of the nanotubes, and decrease with their radius. In the framework of our model, we explain this result by the fact that the carbon atoms are less affected by the repulsive part of the neighborhood's potential as the tube's radius increases, because of the growing inter-atomic distances. In the large-radius limit, the position of the band crossing must be the same as that characterizing isolated graphene sheets. These conclusions also hold for the horizontal position of the band crossing, which appears at 0.656(7), 0.664(7) and 0.666(2) π/a for the (5,5), (10,10) and (15,15) nanotubes respectively (the ideal value predicted by models [35] based on the π-orbital approximation is $\frac{2}{3}\pi/a$).

There is again a good agreement between the bands obtained using the pseudopotential and those given by

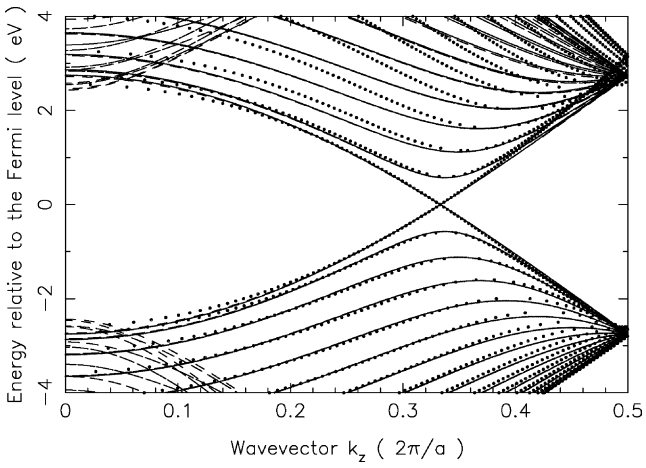

Fig. 9. Band structure of the (15,15) nanotube, as given by tight-binding models, using either the π-orbital approximation (solid) or a complete $sp_xp_yp_z$ basis (dashed), and as calculated using the pseudopotential (dots).

tight-binding models. For the (5,5) our results are actually closer to those provided by the $sp_xp_yp_z$ model, which accounts for the curvature of the tube. As these curvature effects become negligible when considering the (10,10) and (15,15) nanotubes, the $sp_xp_yp_z$ model then reproduces the bands obtained within the π-band approximation and a good general agreement between the three techniques is achieved. As observed previously, it is the hopping parameter γ_0 ($V_{pp\pi}$) of −2.75 eV that gives the best general agreement between the different techniques, while the parameter $\alpha_0 = 2.569$ eV relevant to graphite [23] only improves the matching for the two bands involved by the crossing.

Fig. 10 illustrates the conductance $G(E)$ of eight and 16 basic units of the (5,5) nanotube. The constant metallic plateau in these distributions reflects the linearity of the two bands that cross at the Fermi level. It is delimited by the opening of new bands (with van Hove singularities responsible for the sharp peaks). These band-structure effects are already manifested after propagation through eight units of the tube (i.e., the structure displayed in Fig. 6), and are completely defined after 16 units. The width of the metallic plateau is 3.20 eV, which is close to the value of 3.27 eV given by the tight-binding model of Ref. [38]. As observed with the (10,0) structure, the (5,5) nanotube can accommodate stationary waves, whose number increases with the length of the tube and which are manifested by oscillations in the energy distributions. Similar finite-size effects were observed experimentally by Liang et al. [39].

Looking at the conductance at the Fermi level, one finds that it oscillates as a function of the tube's length (after an initial transition region). This is illustrated in Fig. 11, where we also represented results relevant to the (10,10) and (15,15) nanotubes. One can see that the period of oscillation is $\frac{3}{2}a$, as expected for wave vectors k_z close to $\frac{2}{3}\pi/a$. In the case of the (5,5), one can however observe that the conductance values are not repeated exactly when going from one cycle to the next. This evolution is due to the deviation of the actual value of k_z from the ideal value of $\frac{2}{3}\pi/a$. This effect does not appear for the (10,10) and (15,15) nanotubes, where the corresponding deviations are significantly smaller. Besides addressing these stationary-state solutions, our technique also describes the initial transition where non-propagating states decrease exponentially. One can see that the width of this transition increases with the tube's radius. We explain this behavior by the larger number of states that wide tubes can accommodate (before selection of particular combinations due to band-structure

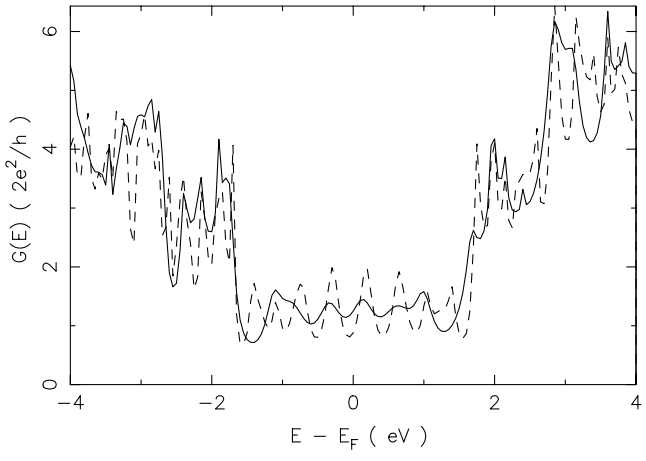

Fig. 10. Conductance of eight (solid) and 16 (dashed) basic units of the (5,5) nanotube. The results account for reflections at the metallic contacts that surround the tubes.

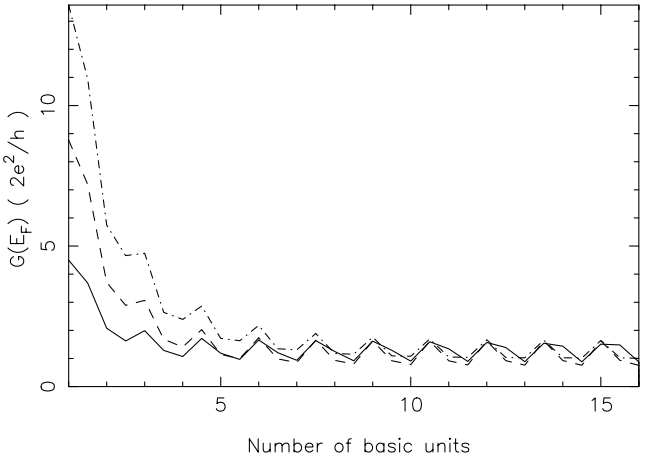

Fig. 11. Conductance at the Fermi level for (5,5) (solid), (10,10) (dashed) and (15,15) (dot-dashed) nanotubes, as a function of the number of basic units. The results account for reflections at the metallic contacts that surround the tubes.

effects). For the (5,5) and (10,10) nanotubes, nine basic units appear sufficient to reach stationary-state conditions (with variations smaller than one percent from one cycle to the next). For the (15,15), 13 units are necessary. Finally one can notice that in all cases the conductance is smaller than the theoretical value of 2 ($2e^2/h$) that characterize infinite nanotubes. In stationary-state conditions, the conductance indeed oscillates between 0.88 and 1.62 for the (5,5), 0.75 and 1.64 for the (10,10), 1.00 and 1.64 for the (15,15). These reduced conductance values come from reflections at the interface between the nanotubes and the metallic contacts.

4.3. Band-structure and transport properties of the (10,10)@(15,15) nanotube

We consider in this section the multi-wall (10,10)@(15,15) structure and investigate how the conductance of a broken (10,10) nanotube is affected by a (15,15) tube placed around the gap. In all cases, D_{5h} configurations are considered in order to preserve the reflection symmetries.

Compared to graphite, the Fermi level of the (10,10)@(15,15) nanotube is 0.425 eV higher. This energy displacement is larger than the 0.11 and 0.075 eV shifts that characterize its single-wall components. In the framework of our model, this is a consequence of the additional repulsive interactions that exist between the layers of multi-wall nanotubes. The band structure of the (10,10)@(15,15) nanotube is represented in Fig. 12. The result is actually the superposition, with a separation of 0.2 eV, of the bands that characterize the isolated tubes. This appears clearly when representing those bands simultaneously. The fact that these bands are only affected by uniform displacements, without avoided-crossing effects, is due to the conservation of reflection symmetries (which cancels any coupling between symmetric and anti-symmetric solutions) [40–42].

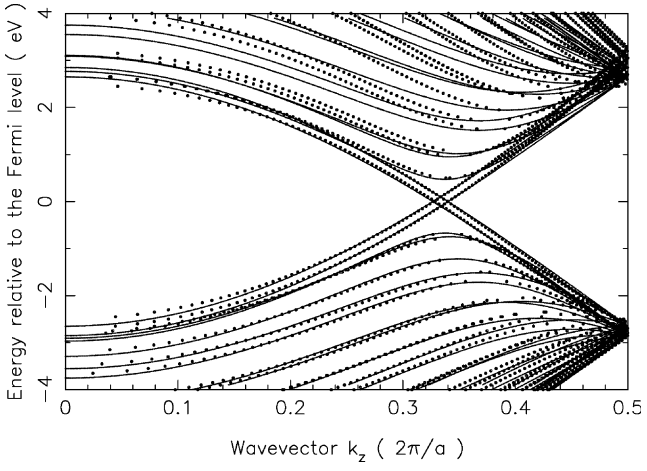

Fig. 12. Band structure of the (10,10)@(15,15) nanotube (in its D_{5h} configuration), as calculated using the pseudopotential (dots). The figure also includes the bands characterizing the (10,10) and (15,15) nanotubes (solid), as obtained within the π-orbital approximation after a shift of 0.1 eV upwards for the (10,10) and downwards for the (15,15).

Fig. 13 illustrates a broken (10,10) nanotube, which consists of 18 units separated symmetrically by a gap whose width is that of a basic cell (0.24595 nm). The gap turns out to be responsible for a reduction of the conductance at the Fermi level $G(E_F)$ from 1.64 to 8.97×10^{-6} ($2e^2/h$). This finite value accounts for electronic tunneling through the gap. Considering a gap three times larger, the conductance $G(E_F)$ reduces to 1.56×10^{-9} ($2e^2/h$). Using a (15,15) nanotube, one can in principle surround the gap and study how the conductance of the broken (10,10) is affected. To provide an example of the systems we consider, we represented in the right part of Fig. 13 the same broken (10,10) tube with seven units of the (15,15). We only consider similar systems, where the (15,15) segment is placed symmetrically around the gap. As the conductance of the two parts of the broken (10,10) tube has a $\frac{3}{2}a$ period and the (15,15) segment is distributed among these two parts, we expect the conductance of the system to oscillate with the length of the (15,15) segment according to a period of $3a$.

We represented in Fig. 14 the conductance of the broken (10,10) nanotube, as a function of the length of the (15,15) segment. The two parts of the representation correspond to a gap length of either one or three basic cells (0.24595 nm), respectively. It appears that the conductance of the broken (10,10) nanotube starts presenting contrasted variations only after the length of the (15,15) segment has become longer than the gap by three units, i.e. for the two cases considered after 4 and 6 units respectively. This minimal length actually corresponds to a $\frac{3}{2}a$ period on each side of the gap. Below this point the conductance only exhibits monotonic variations, while from this point it oscillates with the expected period of $3a$. For the situations considered, the maximal conductance is achieved in the first cycle and corresponds to enhancements of the initial value by two and five orders of magnitude respectively.

5. Conclusion

We described how the transfer-matrix technique can describe periodic materials, providing both scattering solutions and the band structure of these materials. In order to apply this methodology to carbon nanotubes, one had to build a local pseudopotential that represents the carbon atoms and can be used in a one-electron approach. This pseudopotential is interesting in itself, since it enables one to reproduce the π-bands of simple

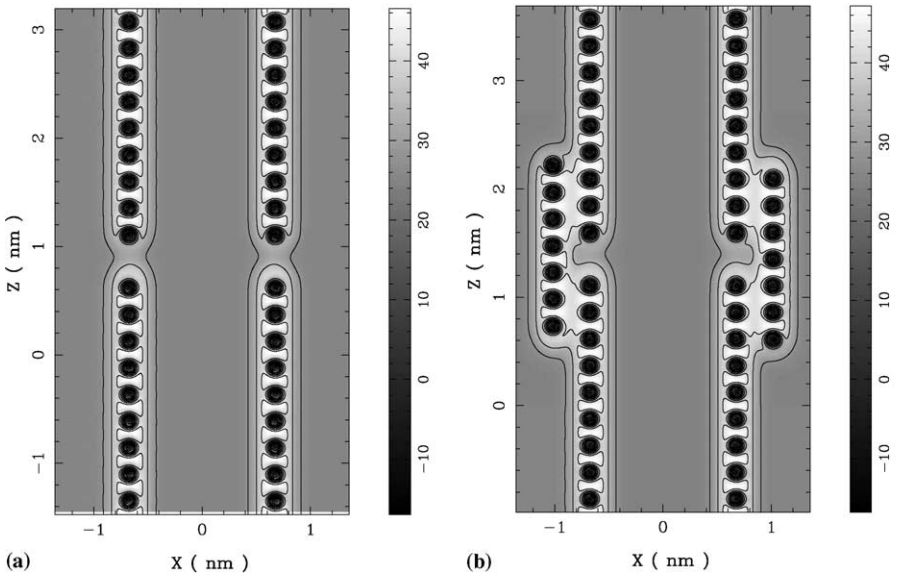

Fig. 13. Potential energy in a broken (10,10) nanotube, without (15,15) (left) and with seven units of the (15,15) (right).

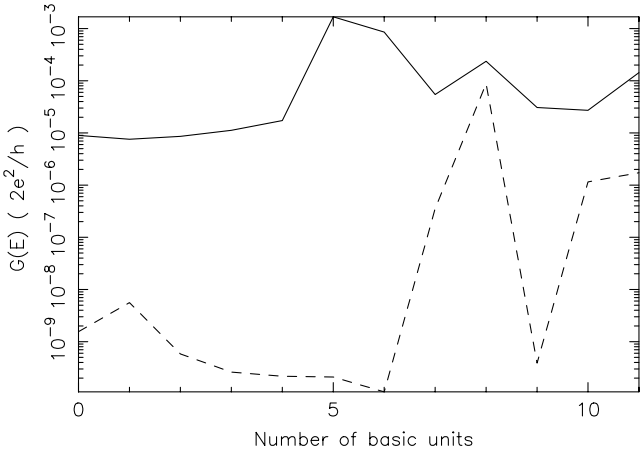

Fig. 14. Conductance of a broken (10,10) nanotube, as a function of the length of the (15,15) segment. The solid and dashed curves correspond to gap lengths of one and three basic cells (0.24595 nm), respectively.

hexagonal graphite, isolated graphene sheets and carbon nanotubes with a reasonable accuracy and using elementary techniques.

The present approach has the advantage to fix the position of the Fermi level, predicting smaller work-function values than in graphite. The variations are of the order of those found in the literature [43] (typically 0.2 eV). In the framework of our model, they are a consequence of the extension of the pseudopotential and the tubes' curvature, which also explains for the band crossing of armchair nanotubes appearing at wave vectors situated slightly below $\frac{2}{3}\pi/a$. Other factors, including charge transfers and σ^*–π^* hybridizations that appear at small radii [44,45], tend to increase the work function [25,26,45,46] but were not considered.

Despite these limitations, the band structures obtained using this technique are in excellent agreement with those provided by tight-binding models and provide some insight on the transferability of parameters from graphite to nanotubes. We could reproduce the π-bands of semiconducting and metallic nanotubes and compute their conductance. These calculations revealed how fast band-structure effects (i.e., band-gaps, constant metallic plateaus and van Hove singularities) appear in finite-size nanotubes. We could also study how the conductance depends on the energy and the tubes' length, thus revealing stationary-wave effects associated with reflections at the metallic contacts. Multi-wall nanotubes were considered and we investigated how the conductance of a broken nanotube is affected by a second tube that surrounds the gap.

The present technique provides an alternative in situations where the density functional theory requires excessive computational resources and the determination of the tight-binding parameters is questionable. The present applications involving multi-wall or broken nanotubes provide examples of such situations. Other examples are the treatment of long, non-periodic structures that contain defects [15] or encapsulated molecules [47], are subject to electric fields (field emission) or constitute only a part of problems where tunneling or ballistic transport outside the nanotube must be described accurately (electron microscopy). The contents of this paper enables one to address these applications and include correct band-structure effects in models that rely on a potential-energy representation of carbon nanotubes.

Acknowledgements

A.M. is supported as Research Associate by the National Fund for Scientific Research (FNRS) of Belgium. The author acknowledges the use of the Namur Scientific Computing Facility and the Belgian State Interuniversity Research Program on *Quantum size effects in nanostructured materials* (PAI/IUAP P5/01). J.-P. Vigneron and Ph. Lambin are acknowledged for useful discussions.

References

[1] Bayman BF, Mehoke CJ. Am J Phys 1983;51(10):875–83.
[2] Tamura H, Ando T. Phys Rev B 1991;44(4):1792–800.
[3] Pendry JB, MacKinnon A. Phys Rev Lett 1992;69(19):2772–5.
[4] Pendry JB. J Mod Opt 1994;41(2):209–29.
[5] Pendry JB. J Phys Condensed Matter 1996;8:1085–8.
[6] Ward AJ, Pendry JB. J Mod Opt 1997;44(9):1703–14.
[7] García-Vidal FJ, Pitarke JM, Pendry JB. Phys Rev B 1998;58:6783–6.
[8] Palacios JJ, Tejedor C. Phys Rev B 1993;48(8):5386–94.
[9] Wu H, Sprung DL. Appl Phys A 1994;58:581–7.
[10] Sheng WD, Xia JB. J Phys Condensed Matter 1994;8:3635–45.
[11] Sheng WD. J Phys Condensed Matter 1997;9:8369–80.
[12] Price PJ. Microelectron J 1999;30:925–34.
[13] Kostyrko T. Phys Rev B 2000;62:2458–65.
[14] Andriotis AN, Menon M, Srivastava D. J Chem Phys 2002;117:2836–43.
[15] Choi HJ, Ihm J. Phys Rev B 1999;59:2267–75.
[16] Mayer A, Vigneron JP. Phys Rev E 1999;59(4):4659–66.
[17] Mayer A, Vigneron JP. Phys Rev E 2000;61(5):5953–60.
[18] Mayer A, Vigneron JP. Phys Rev E 1999;60(6):7533–40.
[19] Mayer A, Vigneron JP. Phys Rev B 1997;56(19):12599–607.
[20] Mayer A, Vigneron JP. J Phys Condensed Matter 1998;10(4):869–81.
[21] Mayer A, Vigneron JP. Phys Rev B 1999;60(4):2875–82.
[22] Mayer A, Vigneron JP. Phys Rev B 2000;62(23):16138–45.
[23] Charlier JC, Michenaud JP, Gonze X. Phys Rev B 1992;46(8):4531–9.
[24] Charlier JC, Michenaud JP, Gonze X, Vigneron JP. Phys Rev B 1991;44(24):13237–49.
[25] Suzuki S, Bower C, Watanabe Y, Zhou O. Appl Phys Lett 2000;76(26):4007–9.
[26] Suzuki S, Watanabe Y, Kiyokura T, Nath KG, Ogino T, Heun S, et al. Phys Rev B 2001;63:245418_1–7.
[27] Kittel CH. Physique de l'état solide. 7th ed. Paris: Dunod; 1998. p. 167–169.
[28] Charlier JC, Gonze X, Michenaud JP. Phys Rev B 1991;43(6):4579–89.
[29] Tabor S, Stafström S. Synth Met 1993;57(2–3):4278–83.
[30] Tanaka A, Onari S, Arai T. Phys Rev B 1993;47(3):1237–43.
[31] Paulsson M, Stafström S. Phys Rev B 1999;60(11):7939–43.
[32] Lázár A, Surján PR, Paulsson M, Stafström S. Int J Quant Chem 2001;84:216–25.
[33] Surján PR, Lázár A, Szabados A. Phys Rev A 2003;68:062503_1–3.
[34] Büttiker M, Imry Y, Landauer R, Pinhas S. Phys Rev B 1985;31(10):6207–15.
[35] Saito R, Fujita M, Dresselhaus G, Dresselhaus MS. Appl Phys Lett 1992;60(18):2204–6.
[36] Moussaddar R, Charlier A, McRae E, Heyd R, Charlier MF. Synth Met 1997;89:81–6.
[37] Ziman JM. Principles of the theory of solids. Cambridge: The University Press; 1964. p. 46–7.
[38] Charlier JC, Lambin Ph. Phys Rev B 1998;57(24):R15037–9.
[39] Liang W, Bockrath M, Bozovic D, Hafner JH, Tinkham M, Park H. Nature 2001;411:665–9.
[40] Saito R, Dresselhaus G, Dresselhaus MS. J Appl Phys 1993;73(2):494–500.
[41] Lambin Ph, Charlier JC, Michenaud JP. In: Kuzmany H, Fink J, Mehring M, editors. Progress in fullerene research. Singapore: World Scientific; 1994 p. 130–4.
[42] Kwon YK, Tománek D. Phys Rev B 1998;58(24):R16001–4.
[43] Chen P, Wu X, Sun X, Lin J, Ji W, Tan KL. Phys Rev Lett 1999;82(12):2548–51.
[44] Blase X, Benedict LX, Shirley EL, Louie SG. Phys Rev Lett 1994;72(12):1878–81.
[45] Miyamoto Y, Saito S, Tomanek D. Phys Rev B 2001;65:041402_1–4.
[46] Zhou G, Duan W, Gu B. Phys Rev Lett 2001;87(9):095504_1–4.
[47] Yoon YG, Mazzoni MSC, Louie SG. Appl Phys Lett 2003;83(25):5217–9.